

Disentangling nucleation and domain growth during a laser-induced phase transition in FeRh

M. Mattern,¹ J. Jarecki,¹ J. A. Arregi,² V. Uhlíř,^{2,3} M. Rössle,⁴ and M. Bargheer^{1,4}

¹*Institut für Physik und Astronomie, Universität Potsdam, 14476 Potsdam, Germany*

²*CEITEC BUT, Brno University of Technology, 61200 Brno, Czech Republic*

³*Institute of Physical Engineering, Brno University of Technology, 61200 Brno, Czech Republic*

⁴*Helmholtz-Zentrum Berlin für Materialien und Energie GmbH,
Wilhelm-Conrad-Röntgen Campus, BESSY II, 12489 Berlin, Germany*

(Dated: May 4, 2023)

We use ultrafast x-ray diffraction and the time-resolved polar magneto-optical Kerr effect to study the laser-induced metamagnetic phase transition in two FeRh films with thicknesses below and above the optical penetration depth. In the thin film, we identify an intrinsic 8 ps timescale for the light-induced nucleation of ferromagnetic domains in the antiferromagnetic material that is substantially slower than the speed of sound. For the inhomogeneously excited thicker film, we additionally identify kinetics of out-of-plane domain growth mediated by near-equilibrium heat transport, which we experimentally verify by comparing Kerr effect experiments in front- and backside excitation geometry.

First-order phase transitions are characterized by an abrupt change of structural, electronic or/and magnetic properties and a co-existence of multiple phases that introduces nucleation and domain growth to the kinetics of the phase transition [1–9].

The abrupt change of properties accompanying the emerging phase as a consequence of a fine interplay of spin, charge, orbital and lattice degrees of freedom [5, 10] predetermine materials featuring first-order phase transitions for ultrafast laser control of functionalities [11]. In this context, the first-order antiferromagnetic to ferromagnetic (AFM-FM) phase transition of FeRh at 370 K attracted considerable attention in terms of ultrafast generation of ferromagnetic order [12, 13] that extends the up to now more extensively studied ultrafast demagnetization [14, 15] and magnetization reversal [16–18].

The metamagnetic phase transition in FeRh is parameterized by the expansion of the unit cell [19], the change in the electronic band structure [20, 21] and the arising magnetization [22, 23], which each serve as order parameters for different aspects of the ultrafast laser-induced phase transition. Time-resolved photoelectron spectroscopy experiments reveal the formation of an electronic signature of the ferromagnetic state by a photo-induced change of the band structure on a sub-picosecond timescale [24], which is proposed to subsequently evolve to a near-equilibrium ferromagnetic state by the formation of a macroscopic magnetization and the relaxation of the lattice on longer timescales. X-ray magnetic circular dichroism [25, 26], magneto-optical Kerr effect (MOKE) [27] and double-pulse THz emission spectroscopy [28] report a formation of an in-plane magnetization on a 100 ps timescale that depends on the excitation fluence [26, 27] and becomes faster with increasing strength of the in-plane magnetic field [28]. Additionally, Li and co-workers very recently proposed a latency in the formation of a local net magnetization due to the required precessional

alignment of the initially antiparallel magnetic moments [28]. The microscopic processes during the laser-induced phase transition are classified as domain nucleation and growth. While the macroscopic magnetization is dominated by the slow coalescence and alignment of the nucleated domains in an external magnetic field [13], the large FM lattice constant as structural order parameter is independent of the orientation of the arising magnetization [27]. Hence, ultrafast x-ray diffraction (UXRD) directly accesses the nucleation and growth of FM domains. Previous UXRD studies report nucleation timescales ranging from 15 to 90 ps depending on the probing depth and fluence [27, 29]. Thus, the kinetics of the nucleation and growth of the laser-induced FM phase remains unclear and controversial.

Here, we disentangle the nucleation of FM domains upon laser-excitation from their out-of-plane growth in near-equilibrium driven by heat diffusion by comparing the transition of the structural order parameter within a homogeneously excited thin FeRh film to an inhomogeneously heated film thicker than the optical penetration depth. In the thin film, we identify a universal fluence- and field-independent 8 ps rise time of the structural order parameter related to the nucleation of FM domains that proceeds slower than the lattice can relax emerging stresses across the thin film at the speed of sound. For the inhomogeneously excited thick film, we observe a distinct fluence dependence with an 8 ps rise time in the low fluence limit and an additional delayed slow rising contribution for high fluences. This additional contribution originates from an out-of-plane growth of the FM domains driven by heat diffusion, which we experimentally verify by time-resolved front- and backside pumping MOKE experiments. Modeling the UXRD results confirms that the domain growth is considerably slower than the heating above the transition temperature. This indicates an additional delay intrinsic to the phase tran-

sition in near equilibrium that deviates from the kinetics of domain nucleation.

The two samples are sketched in Fig. 1(a) and (b) and consist of a 12.6 nm thick FeRh film on MgO(001), and a 43.8 nm thick FeRh film embedded in a metallic heterostructure on MgO(001) consisting of a 2 nm Pt capping and a 8 nm W buffer layer. The thickness of the layers has been characterized via x-ray reflectivity (XRR) and the FeRh films were grown using magnetron sputtering from an equiatomic FeRh target [19]. Both FeRh films exhibit the first-order metamagnetic phase transition characterized by the temperature-dependent magnetization (solid lines) and out-of-plane lattice constant d (symbols) displayed in Fig. 1(c) and (d) for the thin and the thick film, respectively. They were measured in thermal equilibrium via vibrating sample magnetometry (VSM) using a QuantumDesign VersaLab magnetometer and XRD performed at the KMC-3 XPP endstation at BESSY II [30], respectively.

The thin film exhibits a reduced mean transition temperature of $T_T = 365$ K in comparison to the thick film (375 K) and a residual FM phase fraction of around 20% originating from interface effects [31–33]. This reduces the relative expansion associated with the AFM-FM phase transition from 0.6% in the thick film to 0.48% in the thin film. While the magnetization and lattice constant as order parameters of the temperature-induced phase transition nicely agree for the thick film, the inhomogeneity of the thin film results in a narrower hysteresis for the locally probed lattice constant in contrast to the global magnetization determined by VSM.

In the time-resolved combined UXRD and MOKE experiment, the FeRh layers are excited by 100 fs-long p-polarized pump pulses with a central wavelength of 800 nm that are incident under 50° with respect to the sample surface. Utilizing UXRD, we probe the transient out-of-plane strain response of the FeRh layers via reciprocal space mapping [34] of the FeRh(002) Bragg peak at our table-top laser-driven plasma x-ray source [35] providing 200 fs hard x-ray pulses with a photon energy of ≈ 8 keV. The Bragg peak position in reciprocal space is given by the mean out-of-plane lattice constant d of the FeRh films via $q_z = 4\pi/d$. Therefore, the laser-induced peak shift accesses its change Δd determining the lattice strain $\eta_{\text{FeRh}} = \Delta d/d_0$ as the relative change with respect to its value d_0 before excitation. In the very same experimental setup, using the same pump-laser with the same incidence angle, polarization and focusing as in the UXRD experiment, we measured the transient out-of-plane magnetization by polar MOKE with an out-of-plane magnetic field of 1 T provided by an electromagnet. In the combined experiment, we calibrate the fluence inducing the maximum magnetization and the critical excitation threshold to induce a magnetization, which complements the insights of the UXRD measurements. However, the fluence series in Figs. 2 and 3 are recorded at a

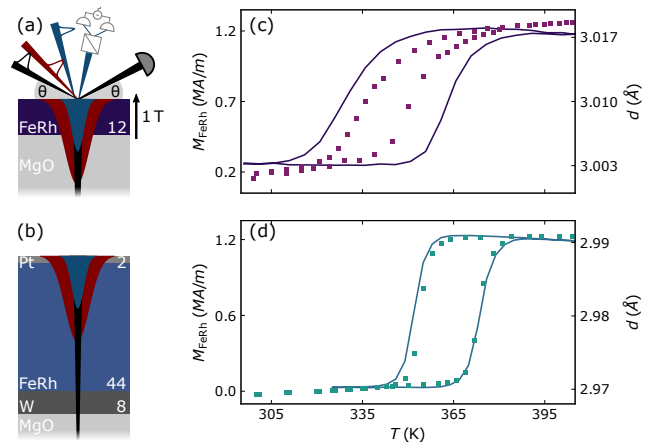


FIG. 1. **Characterization of FeRh films:** (a–b) Sketch of the sample structures containing a 12 nm and a 44 nm FeRh film, the excitation profile (red) and the probing profile of UXRD (black) and MOKE (blue). The combined UXRD and MOKE experiment is sketched in (a). Panels (c) and (d) compare the temperature-dependent magnetization (solid lines) with the out-of-plane lattice constant (symbols) parametrizing the AFM-FM phase transition in the thin and thick FeRh film, respectively.

separated signal-to-noise ratio optimized set-up [36] with the pump-pulse at normal incidence, where we rescale the fluence values according to the MOKE results in the combined experiment.

Figure 2(a) displays the fluence-dependent out-of-plane strain response of the thin FeRh film. Exemplarily for the fluence of 1.8 mJ/cm^2 , we show the comparison of the strain response for an applied out-of-plane magnetic field of 1 T (squares) and without external field (dots). The sub-threshold fluence of $F_{\text{st}} = 0.5 \text{ mJ/cm}^2$ does not induce the phase transition, which is confirmed by the absence of a laser-induced magnetization probed by MOKE in panel (c). Under this condition, the strain response is the superposition of a quasi-static expansion due to heating and a coherently driven propagating strain pulse reflected at the surface and the interface, where it is partially transmitted into the substrate. The resulting expansion decays within hundreds of picoseconds due to heat transport into the substrate. A superimposed decaying oscillation with a period of $2L_{\text{FeRh}}/v_s$ is determined by the layer thickness L_{FeRh} and the sound velocity v_s [37]. These thermoelastic strain contributions scale linearly with the energy deposited in the electron-phonon system. Using the modular PYTHON library UDKM1DSIM [38] and literature values for thermoelastic properties stated in Tab. S1 (see supplementary material also for a detailed description of the modelling) we match the measured strain for sub-threshold excitation ($F_{\text{st}} = 0.5 \text{ mJ/cm}^2$). The dashed line in Fig. 2(a) represents the modeled thermoelastic strain scaled to 2.1 mJ/cm^2 , i.e. the hypothetical strain response without

phase transition. The difference to the actual measurement determines the transient contribution of the AFM-FM phase transition to the strain. From this we calculate the ferromagnetic volume fraction V_{FM} in Fig. 2(b) for the three fluences above threshold by relating a full phase transition to an additional expansion of 0.48% as in equilibrium. To obtain good agreement of the model including the AFM-FM phase transition (solid lines) with the super-threshold strain response, we had to consider that the energy consumed by the latent heat of the phase transition indeed does not contribute to thermoelastic expansion. In addition, we assume the thermal expansion coefficient in the arising FM volume fraction to have the characteristic high temperature value (Tab. S1).

We observe that the extracted FM volume fraction rises as a single exponential according to:

$$V_{\text{FM}}(t) = V_{\text{FM}}^* \cdot \left(1 - e^{-t/\tau}\right), \quad (1)$$

where V_{FM}^* denotes the final fraction of the film in the FM phase and τ is the rise time. With increasing fluence, we observe an increase of V_{FM}^* that saturates at a fluence $F_{\text{sat}} = 2.1 \text{ mJ/cm}^2$ when the complete film is driven into the FM phase which also causes the maximum magnetization observed in the MOKE experiment (Fig. 2(c)). For the rise time of V_{FM} associated with the nucleation of FM domains at independent sites [1, 27], we observe a universal $\tau = 7.8 \pm 0.6 \text{ ps}$ timescale from the fit of all measurements in Fig. 2(b). This is clearly slower than the relaxation of the lattice: The propagation of strain pulses through the thin film at the speed of sound only takes 2.5 ps (cf. Fig. 2(a)). This highlights a fluence- and field-independent nucleation of FM domains representing intrinsic kinetics of the phase transition. Afterwards, the in-plane magnetization of the FM domains precessionally aligns with the out-of-plane field. The out-of-plane magnetization reaches its maximum at $\approx 180 \text{ ps}$ independent of the fluence (see Fig. 2(c)). Panels (d–h) sketch this series of events that starts with the ultrafast demagnetization of the residual FM phase within the first picoseconds. The pink fraction of the film represents V_{FM} and the magnetization direction is indicated by arrows.

In the case of the thick FeRh film, whose thickness exceeds the optical penetration depth, the redistribution of energy within the layer by heat transport extends the dynamics from mainly two dimensional in case of the homogeneously excited thin film to three dimensional because the induced FM phase starts extending along the out-of-plane direction. We again extract the FM volume fraction from the fluence-dependent transient strain response in Fig. 3(a) by subtracting the appropriately scaled response to a sub-threshold excitation F_{st} . Our model of the laser-induced AFM strain matches the sub-threshold strain response of FeRh and calibrates the laser-induced spatio-temporal temperature that is cross-checked by an additional excellent agreement to the transient strain

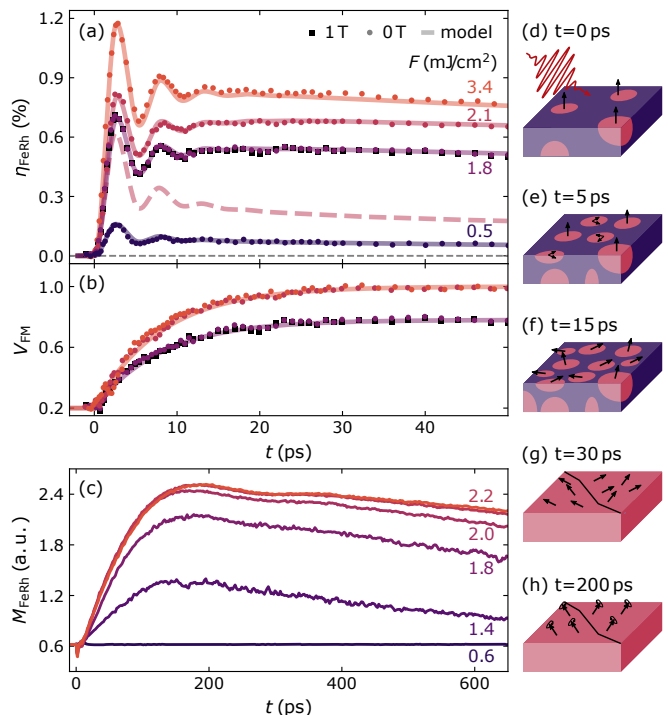


FIG. 2. **Universal timescale of nucleation:** (a) Fluence-dependent strain response of the 12 nm thick FeRh film (dots) and modeled transient strain (solid lines) considering the quasi-static expansion, propagating strain pulses and the expansion caused by the AFM-FM phase transition. The dashed line is the modeled strain for 0.5 mJ/cm^2 scaled to 2.1 mJ/cm^2 , i.e. the hypothetical response without phase transition. (b) Transient FM volume fraction extracted from the difference between measured and modeled strain response without phase transition (dashed line in (a)) normalized to the expansion across the phase transition in thermal equilibrium. (c) Fluence-dependent transient out-of-plane magnetization from polar MOKE. Panels (d–h) sketch the kinetics of the phase transition in regard of the structural order parameter (pink color) and the magnetization (arrows).

measured in the adjacent W layer (see Fig. S1).

Figure 3(b) displays the change from a single exponential rise of V_{FM} for low fluences to a two-step rise for high fluences ($> 6 \text{ mJ/cm}^2$). Irrespective of the fluence, V_{FM} rises as a single exponential during the first 30 ps according to Eq. (1) (solid colored lines) with the 8 ps nucleation timescale identified in the thin film. This highlights the universality of the kinetics of domain nucleation during the AFM-FM phase transition, which is independent of the sample structure and the excitation fluence. In the high fluence regime, we observe an additional delayed slow rise of the FM volume fraction. With increasing fluence, the amplitude of the second contribution increases but the maximum FM volume fraction is reached at later delays up to 250 ps for the highest fluence driving the complete FeRh film across the AFM-FM phase transition. For front-side laser excitation, the rise

of the magnetization (Fig. 3(c)) is independent of the fluence (see normalized results in Fig. S3 in the supplement), as already observed for the thin film. For backside excitation geometry in contrast, the rise of the magnetization probed at the front surface (Fig. 3(d)) slows down with decreasing fluence. This fluence dependence indicates that the second slower contribution to the rise of V_{FM} must originate from an out-of-plane growth of the FM domains driven by heating increasing fractions of the FeRh film above T_{T} via near-equilibrium heat transport.

The equilibration of the phonon temperature after sub-picosecond electron-phonon coupling within the inhomogeneously excited FeRh layer (optical penetration depth $\lambda = 13$ nm) causes a delayed slow heating of the backside via heat diffusion. In the low fluence regime (< 6 mJ/cm²), the phonon temperature at the backside is insufficient to drive the phase transition. For high fluences, sufficient energy is transported towards the substrate to increase the phonon temperature at the backside of the FeRh film beyond the transition temperature, thus enabling the phase transition in near-equilibrium. This results in the two-step rise of V_{FM} for high fluences. For initial sample temperatures only slightly below T_{T} , the same two-step behavior is demonstrated by the temperature series in Fig. S2 in the supplementary material. This experiment was performed at the KMC-3 XPP endstation at BESSY II in the low-alpha operation mode [30], where the excellent collimation of the synchrotron beam allows for separating the Bragg peaks of the FM and AFM phases. This enables a direct extraction of ferromagnetic volume fraction V_{FM} by accessing the transient change of the relative amplitudes of the two Bragg peaks similar to the report by Mariager and co-workers [27].

The acceleration of the magnetization rise in backside excitation geometry with increasing fluence (Fig. 3(d)) as well as the fluence-dependent maximum magnetization in combination with the delayed maximum V_{FM} in the UXRD experiment for high fluences (Fig. 3b) indicate that the nucleated FM domains grow into the depth of the FeRh film as sketched in panels (e–h) in the low (dark green) and high (bright green) fluence limit. Our interpretation is supported by the decreasing maximum FM volume fraction with increasing x-ray probing depth reported by Mariager and co-workers [27]. This differs from the formation of columns through the FeRh film after the nucleation of FM domains at both interfaces in homogeneous equilibrium heating [2], because the inhomogeneous excitation in our experiment results in the nucleation of FM domains only in the near-surface region and a delayed heating of the backside of the FeRh film.

The modeled spatio-temporal temperature provides additional insights into the domain growth within the inhomogeneously excited FeRh layer. The grey solid line in Fig. 3(b) denotes the fraction V_{T} of the film transiently heated above the mean transition temperature of 375 K considering the latent heat of the phase transi-

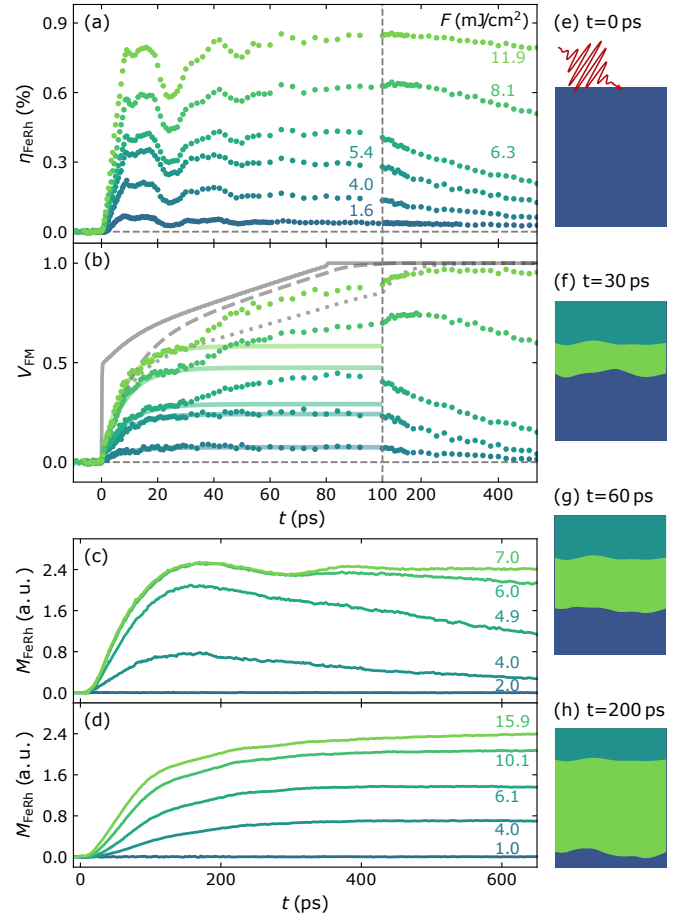


FIG. 3. **Kinetics of out-of-plane domain growth:** (a) Fluence-dependent field-free strain response of the 44 nm thick FeRh film. (b) Transient FM volume fraction derived analogously to the thin film by comparing the measured strain to a scaled sub-threshold fluence model. Panels (c) and (d) display the fluence-dependent magnetization rise measured by polar MOKE with a magnetic field of 1 T in front- and backside excitation geometry, respectively. (e–h) Sketch of the out-of-plane growth of the FM phase indicated by the green area for 5.4 (left) and 11.9 mJ/cm² (right) that is induced by a fluence-dependent heating above T_{T} at the backside via near-equilibrium heat transport.

tion for an excitation of 11.9 mJ/cm². The transient V_{T} highlights, that already within the first 30 ps a considerably large fraction of the film is heated above T_{T} by heat diffusion and that the complete film is heated above the mean transition temperature within 80 ps. This is much faster than the rise of V_{FM} taking 250 ps and indicates that the domain growth does not simply follow the heating of the backside above T_{T} but exhibits intrinsic kinetics. If we assume the rise of the FM phase with an 8 ps timescale after a unit cell is heated above T_{T} (grey dashed line), the modelled rise of V_{FM} is still significantly faster than in the measurement. This highlights the different kinetics of nucleation and domain growth for the AFM-FM phase transition in FeRh. Finally, the grey

dotted line represents the combination of an 8 ps nucleation timescale for the optically heated unit cells and a second 50 ps timescale for the formation of the FM phase for unit cells heated above T_T by heat transport. This approach matches the delay when V_{FM}^* is reached but is not in agreement with the measurement between 30 and 100 ps. This suggests that the domain growth into the depth of the film only starts after the nucleation of the FM domains in the optically excited near-surface-region is finished after 30 ps (see Fig. 3(b)) even though a large fraction of the layer is already heated above the equilibrium transition temperature.

In summary, we discovered a universal fluence- and field-independent 8 ps timescale for the optically driven nucleation of FM domains in our UXRd experiment. This timescale is not limited by the relaxation of the lattice with sound velocity as stated previously [27] but represents intrinsic kinetics of the first-order phase transition. The comparison of the homogeneously excited thin FeRh film with the inhomogeneously excited thick FeRh layer reveals an additional delayed and much slower transition of the structural order parameter in the high fluence regime. Utilizing the near surface sensitivity of MOKE and comparing front- and backside excitation we show that this additional contribution originates from an out-of-plane growth of the nucleated FM domains induced by a heating above the transition temperature at the backside of the film via heat transport in near-equilibrium. Our analysis considering the modeled spatio-temporal temperature reveals different intrinsic kinetics of optically induced nucleation and near-equilibrium heating-induced domain growth that seems to start after the nucleation is finished. These findings should be considered in future investigations of the kinetics of magnetization formation upon laser excitation that started very recently [28].

We acknowledge the DFG for financial support via No. BA 2281/11-1 and Project-No. 328545488 – TRR 227, project A10. Access to the CEITEC Nano Research Infrastructure was supported by the Ministry of Education, Youth and Sports (MEYS) of the Czech Republic under the project CzechNanoLab (LM2018110).

-
- [1] M. Avrami, Kinetics of phase change. i general theory, *The Journal of chemical physics* **7**, 1103 (1939).
- [2] C. Gatel, B. Warot-Fonrose, N. Biziere, L. Rodríguez, D. Reyes, R. Cours, M. Castiella, and M.-J. Casanove, Inhomogeneous spatial distribution of the magnetic transition in an iron-rhodium thin film, *Nature Communications* **8**, 15703 (2017).
- [3] V. Uhlř, J. A. Arregi, and E. E. Fullerton, Colossal magnetic phase transition asymmetry in mesoscale ferri stripes, *Nature communications* **7**, 13113 (2016).
- [4] S. Roy, G. Perkins, M. Chattopadhyay, A. Nigam, K. Sokhey, P. Chaddah, A. Caplin, and L. Cohen, First order magnetic transition in doped ceFe 2 alloys: Phase coexistence and metastability, *Physical review letters* **92**, 147203 (2004).
- [5] S. De Jong, R. Kukreja, C. Trabant, N. Pontius, C. Chang, T. Kachel, M. Beye, F. Sorgenfrei, C. Back, B. Bräuer, *et al.*, Speed limit of the insulator–metal transition in magnetite, *Nature materials* **12**, 882 (2013).
- [6] F. Randi, I. Vergara, F. Novelli, M. Esposito, M. Dell’Angela, V. Brabers, P. Metcalf, R. Kukreja, H. A. Dürr, D. Fausti, *et al.*, Phase separation in the nonequilibrium verwey transition in magnetite, *Physical Review B* **93**, 054305 (2016).
- [7] M. M. Qazilbash, M. Brehm, B.-G. Chae, P.-C. Ho, G. O. Andreev, B.-J. Kim, S. J. Yun, A. Balatsky, M. Maple, F. Keilmann, *et al.*, Mott transition in vo2 revealed by infrared spectroscopy and nano-imaging, *Science* **318**, 1750 (2007).
- [8] C. Baldasseroni, C. Bordel, A. Gray, A. Kaiser, F. Kronast, J. Herrero-Albillos, C. Schneider, C. Fadley, and F. Hellman, Temperature-driven nucleation of ferromagnetic domains in ferri thin films, *Applied Physics Letters* **100**, 262401 (2012).
- [9] D. J. Keavney, Y. Choi, M. V. Holt, V. Uhlř, D. Arena, E. E. Fullerton, P. J. Ryan, and J.-W. Kim, Phase coexistence and kinetic arrest in the magnetostructural transition of the ordered alloy ferri, *Scientific reports* **8**, 1778 (2018).
- [10] S. Polesya, S. Mankovsky, D. Ködderitzsch, J. Minár, and H. Ebert, Finite-temperature magnetism of ferri compounds, *Physical Review B* **93**, 024423 (2016).
- [11] D. Wegkamp, M. Herzog, L. Xian, M. Gatti, P. Cudazzo, C. L. McGahan, R. E. Marvel, R. F. Haglund Jr, A. Rubio, M. Wolf, *et al.*, Instantaneous band gap collapse in photoexcited monoclinic vo 2 due to photocarrier doping, *Physical review letters* **113**, 216401 (2014).
- [12] G. Ju, J. Hohlfeld, B. Bergman, R. J. van de Veerdonk, O. N. Mryasov, J.-Y. Kim, X. Wu, D. Weller, and B. Koopmans, Ultrafast generation of ferromagnetic order via a laser-induced phase transformation in ferri thin films, *Physical review letters* **93**, 197403 (2004).
- [13] B. Bergman, G. Ju, J. Hohlfeld, R. J. van de Veerdonk, J.-Y. Kim, X. Wu, D. Weller, and B. Koopmans, Identifying growth mechanisms for laser-induced magnetization in ferri, *Physical Review B* **73**, 060407 (2006).
- [14] E. Beaurepaire, J.-C. Merle, A. Daunois, and J.-Y. Bigot, Ultrafast spin dynamics in ferromagnetic nickel, *Physical review letters* **76**, 4250 (1996).
- [15] A. Kirilyuk, A. V. Kimel, and T. Rasing, Ultrafast optical manipulation of magnetic order, *Reviews of Modern Physics* **82**, 2731 (2010).
- [16] C. D. Stanciu, F. Hansteen, A. V. Kimel, A. Kirilyuk, A. Tsukamoto, A. Itoh, and T. Rasing, All-optical magnetic recording with circularly polarized light, *Physical review letters* **99**, 047601 (2007).
- [17] I. Radu, K. Vahaplar, C. Stamm, T. Kachel, N. Pontius, H. Dürr, T. Ostler, J. Barker, R. Evans, R. Chantrell, *et al.*, Transient ferromagnetic-like state mediating ultrafast reversal of antiferromagnetically coupled spins, *Nature* **472**, 205 (2011).
- [18] Q. Remy, J. Hohlfeld, M. Vergès, Y. Le Guen, J. Gorchon, G. Malinowski, S. Mangin, and M. Hehn, Accelerating ultrafast magnetization reversal by non-local spin transfer, *Nature Communications* **14**, 445 (2023).

- [19] J. A. Arregi, O. Caha, and V. Uhlř, Evolution of strain across the magnetostructural phase transition in epitaxial ferh films on different substrates, *Physical Review B* **101**, 174413 (2020).
- [20] A. Gray, D. Cooke, P. Krüger, C. Bordel, A. Kaiser, S. Moyerman, E. Fullerton, S. Ueda, Y. Yamashita, A. Gloskovskii, *et al.*, Electronic structure changes across the metamagnetic transition in ferh via hard x-ray photoemission, *Physical review letters* **108**, 257208 (2012).
- [21] F. Pressacco, V. Uhlř, M. Gatti, A. Nicolaou, A. Bendounan, J. A. Arregi, S. K. Patel, E. E. Fullerton, D. Krizmancic, and F. Sirotti, Laser induced phase transition in epitaxial ferh layers studied by pump-probe valence band photoemission, *Structural Dynamics* **5**, 034501 (2018).
- [22] S. Maat, J.-U. Thiele, and E. E. Fullerton, Temperature and field hysteresis of the antiferromagnetic-to-ferromagnetic phase transition in epitaxial ferh films, *Physical Review B* **72**, 214432 (2005).
- [23] C. Stamm, J.-U. Thiele, T. Kachel, I. Radu, P. Ramm, M. Kosuth, J. Minár, H. Ebert, H. Dürr, W. Eberhardt, *et al.*, Antiferromagnetic-ferromagnetic phase transition in ferh probed by x-ray magnetic circular dichroism, *Physical Review B* **77**, 184401 (2008).
- [24] F. Pressacco, D. Sangalli, V. Uhlř, D. Kutnyakhov, J. A. Arregi, S. Y. Agustsson, G. Brenner, H. Redlin, M. Heber, D. Vasilyev, *et al.*, Subpicosecond metamagnetic phase transition in ferh driven by non-equilibrium electron dynamics, *Nature Communications* **12**, 5088 (2021).
- [25] A. Ünal, A. Parabas, A. Arora, J. Ehrler, C. Barton, S. Valencia, R. Bali, T. Thomson, F. Yildiz, and F. Kronast, Laser-driven formation of transient local ferromagnetism in ferh thin films, *Ultramicroscopy* **183**, 104 (2017).
- [26] I. Radu, C. Stamm, N. Pontius, T. Kachel, P. Ramm, J.-U. Thiele, H. Dürr, and C. Back, Laser-induced generation and quenching of magnetization on ferh studied with time-resolved x-ray magnetic circular dichroism, *Physical Review B* **81**, 104415 (2010).
- [27] S. O. Mariager, F. Pressacco, G. Ingold, A. Caviezel, E. Möhr-Vorobeva, P. Beaud, S. Johnson, C. Milne, E. Mancini, S. Moyerman, *et al.*, Structural and magnetic dynamics of a laser induced phase transition in ferh, *Physical Review Letters* **108**, 087201 (2012).
- [28] G. Li, R. Medapalli, J. Mentink, R. Mikhaylovskiy, T. Blank, S. Patel, A. Zvezdin, T. Rasing, E. Fullerton, and A. Kimel, Ultrafast kinetics of the antiferromagnetic-ferromagnetic phase transition in ferh, *Nature Communications* **13**, 2998 (2022).
- [29] F. Quirin, M. Vattilana, U. Shymanovich, A.-E. El-Kamhawy, A. Tarasevitch, J. Hohlfeld, D. von der Linde, and K. Sokolowski-Tinten, Structural dynamics in ferh during a laser-induced metamagnetic phase transition, *Physical Review B* **85**, 020103 (2012).
- [30] M. Rössle, W. Leitenberger, M. Reinhardt, A. Koç, J. Pudell, C. Kwamen, and M. Bargheer, The time-resolved hard x-ray diffraction endstation kmc-3 xpp at bessy ii, *Journal of Synchrotron Radiation* **28**, 948 (2021).
- [31] F. Pressacco, V. Uhlř, M. Gatti, A. Bendounan, E. E. Fullerton, and F. Sirotti, Stable room-temperature ferromagnetic phase at the ferh (100) surface, *Scientific reports* **6**, 22383 (2016).
- [32] R. Fan, C. J. Kinane, T. Charlton, R. Dorner, M. Ali, M. De Vries, R. M. Brydson, C. H. Marrows, B. J. Hickey, D. A. Arena, *et al.*, Ferromagnetism at the interfaces of antiferromagnetic ferh epilayers, *Physical Review B* **82**, 184418 (2010).
- [33] X. Chen, J. Feng, Z. Wang, J. Zhang, X. Zhong, C. Song, L. Jin, B. Zhang, F. Li, M. Jiang, *et al.*, Tunneling anisotropic magnetoresistance driven by magnetic phase transition, *Nature Communications* **8**, 449 (2017).
- [34] D. Schick, R. Shayduk, A. Bojahr, M. Herzog, C. v. Korff Schmising, P. Gaal, and M. Bargheer, Ultrafast reciprocal-space mapping with a convergent beam, *Journal of Applied Crystallography* **46**, 1372 (2013).
- [35] D. Schick, A. Bojahr, M. Herzog, C. v. K. Schmising, R. Shayduk, W. Leitenberger, P. Gaal, and M. Bargheer, Normalization schemes for ultrafast x-ray diffraction using a table-top laser-driven plasma source, *Review of Scientific Instruments* **83**, 025104 (2012).
- [36] L. Willig, A. von Reppert, M. Deb, F. Ganss, O. Hellwig, and M. Bargheer, Finite-size effects in ultrafast remagnetization dynamics of fept, *Physical Review B* **100**, 224408 (2019).
- [37] M. Mattern, A. von Reppert, S. P. Zeuschner, J.-E. Pudell, M. Herzog, and M. Bargheer, Concepts and use cases for picosecond ultrasonics with x-rays, arXiv preprint arXiv:2302.14116 10.48550/ARXIV.2302.14116 (2023).
- [38] D. Schick, udkm1dsim—a python toolbox for simulating 1d ultrafast dynamics in condensed matter, *Computer Physics Communications* **266**, 108031 (2021).

Supplementary material to: Disentangling nucleation and domain growth during a laser-induced phase transition in FeRh

M. Mattern,¹ J. Jarecki,¹ J. A. Arregi,² V. Uhlíř,^{2,3} M. Rössle,⁴ and M. Bargheer^{1,4}

¹*Institut für Physik und Astronomie, Universität Potsdam, 14476 Potsdam, Germany*

²*CEITEC BUT, Brno University of Technology, 61200 Brno, Czech Republic*

³*Institute of Physical Engineering, Brno University of Technology, 61200 Brno, Czech Republic*

⁴*Helmholtz-Zentrum Berlin für Materialien und Energie GmbH, Wilhelm-Conrad-Röntgen Campus, BESSY II, 12489 Berlin, Germany*

(Dated: May 4, 2023)

S1. THERMO-ELASTIC STRAIN MODEL

In this section, we describe the procedure of modeling the transient strain response by using the modular PYTHON library UDKM1DSIM [1] and the layer-specific thermo-elastic parameters given in Tab. S1. In general, the UDKM1DSIM library captures the entire series of events in ultrafast x-ray diffraction (UXRD) experiments from the optically deposited energy density to the calculation of a Bragg peak shift via dynamical x-ray diffraction theory.

In our model approach, we do not individually treat electron and phonon degrees of freedom within the framework of a two-temperature model (2TM) since the literature does not provide separate values for the heat conductivity of electrons and phonons, their coupling and the electronic contribution to the thermal expansion in FeRh. Instead, our model only contains a single temperature that corresponds to the phonon temperature after electron-phonon equilibration in a 2TM. The initial temperature profile within the samples is determined by the optical penetration depth λ and the macroscopic heat capacity C_{ph} . The subsequent equilibration of the temperature across the metallic stack and the cooling towards the substrate determines the spatio-temporal temperature increase $\Delta T(z, t)$ by solving the diffusion equation accounting for the layer-specific heat capacities C_{ph} and thermal conductivities κ . The temperature increase determines the laser-induced stress $\sigma^{\text{ext}}(t) = c_{3333} \cdot \alpha_{\perp}^{\text{uf}} \cdot \Delta T(t)$ on ultrafast (uf) timescales via the expansion coefficient $\alpha_{\perp}^{\text{uf}}$ that accounts for the exclusive out-of-plane strain response of the metallic films and is calculated by

| | Pt | FeRh | W | MgO |
|--|------------|-------------------------------|-------------|---------------------|
| unit cell orientation | (111) | (001) | (001) | (001) |
| number of simulated unit cells | | | | |
| thin film | - | 42 (12.6 nm) | - | substrate |
| thick film | 8 (1.8 nm) | 146 (43.8 nm) | 28 (8.9 nm) | substrate |
| density ρ (g cm ⁻³) | 21.45 | 9.93 | 19.25 | 3.58 |
| elastic constants (GPa) | from [2] | from [3] | from [4] | from [5] |
| c_{3333} | 386 | 285 | 523 | 289.3 |
| c_{1133} | 232 | 136 | 204 | 87.7 |
| c_{2233} | 232 | 136 | 204 | 87.7 |
| out-of-plane sound velocity v_s (nm ps ⁻¹) | 4.24 | <u>5.00</u> (5.31) | 5.21 | 9.12 |
| lin. therm. expansion α (10 ⁻⁶ K ⁻¹) | 8.9 [6] | 9.7 (AFM) [7] 6.0 (FM) [7] | 4.6 [6] | 10.5 [8] |
| lin. therm. expansion $\alpha_{\perp}^{\text{uf}}$ (10 ⁻⁶ K ⁻¹) | 19.6 | 19.6 (AFM) 12.4 (FM) | 8.2 | 16.9 |
| Grüneisen parameter of electrons Γ_{el} | 1.4 [9] | <u>1.4</u> | <u>1.4</u> | - |
| Grüneisen parameter of phonons Γ_{ph} | 2.6 | 1.7 | 1.6 | 1.7 |
| electron-phonon coupling time $\tau_{\text{el-ph}}$ (ps) | 0.4 [10] | <u>0.6</u> | 0.6 [11] | - |
| heat capacity C_{ph} (Jkg ⁻¹ K ⁻¹) | 133 [12] | 350 [13] | 132 [14] | 928 [15] |
| heat conductivity κ (W m ⁻¹ K ⁻¹) | | | | |
| thin film | - | 50 [16] | - | <u>20</u> (50 [17]) |
| thick film | 71 [18] | <u>25</u> (50 [16]) | 170 [19] | <u>20</u> (50 [17]) |
| optical penetration depth λ (nm) | | | | |
| thin film | - | multilayer [20] | - | inf |
| thick film | <u>13</u> | <u>13</u> | <u>8</u> | inf |

TABLE S1. Thermo-elastic parameters of Pt, FeRh, W and the MgO substrate taken from the literature. Underlined values are optimized in the model to match the observed results. If literature values are available they are provided in parentheses.

$\alpha_{\perp}^{\text{uf}} = (1 + \frac{c_{1133} + c_{2233}}{c_{3333}}) \cdot \alpha$ considering the isotropic expansion coefficient α of bulk specimen [21]. The stress $\sigma^{\text{ext}}(t)$ drives the spatio-temporal strain response $\eta(z, t)$ as a superposition of a quasi-static expansion and coherently driven propagating strain pulses determined by numerically solving the one-dimensional inhomogeneous elastic wave equation. Finally, the UDKM1DSIM library calculates Bragg peaks for each layer considering $\eta(z, t)$ via dynamical x-ray diffraction theory. Their transient shift is compared to the UXRD measurements.

The values used for the layer-specific thermo-elastic parameters involved in the model process mainly taken from the literature are stated in Tab. S1. Adjusted values are underlined in the table. In addition to the sequence described above, we include a finite stress rise time. In a one-temperature model this corresponds to a phenomenological electron-phonon coupling time $\tau_{\text{el-ph}}$, which mimics the solution of a 2TM. The different electronic and phononic Grüneisen parameters (Γ_{el} and Γ_{ph}) parametrize the efficiency of stress generation by energy deposition to the respective degree of freedom. Thus, we re-scale the temperature (energy) increase calculated from the heat diffusion equation by $(1 - \frac{\Gamma_{\text{ph}} - \Gamma_{\text{el}}}{\Gamma_{\text{ph}}}) \cdot e^{-t/\tau_{\text{el-ph}}}$ describing the corresponding stress rise. The phononic Grüneisen parameters are calculated from the thermal expansion via $\Gamma_{\text{ph}} = \alpha_{\perp}^{\text{uf}} \frac{c_{3333}}{C_{\text{ph}} \cdot \rho}$ and the electronic Grüneisen parameters are taken from the literature or optimized to match the shape and amplitude of the propagating strain pulses. The electron-phonon coupling timescale $\tau_{\text{el-ph}}$ in FeRh is estimated from transient reflectivity measurements. Furthermore, we determine the optical penetration depth of the thick sample by matching the shape of the strain pulse, especially the shape of the rapidly rising compression of the W buffer layer. In contrast, in the thin film we use a transfer-matrix formalism to calculate the absorption in terms of a multilayer model using literature values for the complex refractive index of FeRh [20] and MgO. To match the slow cooling of the optically excited FeRh layer towards W and the MgO substrate in Fig. S1, we reduce the heat conductivity of the FeRh film. We find the same quality of agreement with the data if we take the literature value for the heat conductivity in FeRh but reduce the heat conductivity of the first unit cell of W to 2 W/Km to model a large interface resistance. Under this assumption, the equilibration of the temperature within the FeRh layer would be even faster. This equally well supports the conclusion in the main text that the domain growth is considerably delayed with respect to the heating above T_T .

S2. DETERMINATION OF SPATIO-TEMPORAL TEMPERATURE WITHIN THE THICK FeRh FILM

In this section, we display the comparison of the measured strain response of FeRh to a sub-threshold fluence and the modeled strain response that serves as a reference to extract the transient ferromagnetic volume fraction V_{FM} from the strain response to super-threshold excitations in the main text. Furthermore, it yields $\Delta T(z, t)$ that we use as a reference to identify the intrinsic kinetics of domain growth upon heating above the transition temperature.

Figure S1(a) and (b) display the modeled transient strain response of the FeRh layer to an excitation of 1.6 mJ/cm^2 and the W buffer layer for a fluence of 6.3 mJ/cm^2 , respectively. The model utilizes the same set of thermo-elastic parameters stated in Tab. S1 for both layers and neglects any contributions from the antiferromagnetic-to-ferromagnetic (AFM-FM) phase transition, i.e. exclusively describes the strain response typical of metallic transducers [21]. Figure S1(c) and (d) display the underlying calculated spatio-temporal temperature increase and strain for 1.6 mJ/cm^2 , respectively. The spatio-temporal strain displays a bipolar strain pulse with leading compression driven at the optically excited surface of the sample that subsequently propagates through the FeRh layer into the W buffer layer and the MgO substrate. The compressive part of the strain pulse entering the W layer causes the observed initial compression of W. The maximum expansion of FeRh occurs at 9 ps, when the prevailing expansive part enters W leading to an expansion. The partial reflection of the strain pulse at the W-MgO interface, which is poorly impedance matched, causes a decaying oscillation of the strain in FeRh with a complex shape due to the heterostructure nature of the sample.

The good agreement of our model with both the shape of the coherently driven propagating strain pulses and the transient quasi-static expansion on long timescales in FeRh and W verifies both the initial inhomogeneous distribution of the optically deposited energy density and the subsequent redistribution within the FeRh layer via heat diffusion, which serve as a reference for the insights into the kinetics of the out-of-plane domain growth in the main text. Furthermore, we find a good agreement with the slowly rising expansion of W by heat transport from FeRh into W for a fluence of 6.3 mJ/cm^2 , which already drives the AFM-FM phase transition in FeRh. This highlights that the heat transport and therefore the spatio-temporal temperature within FeRh is in first-order approximation not influenced by the growing FM phase despite the reported reduced electric conductivity by magnetoresistance measurements[22].

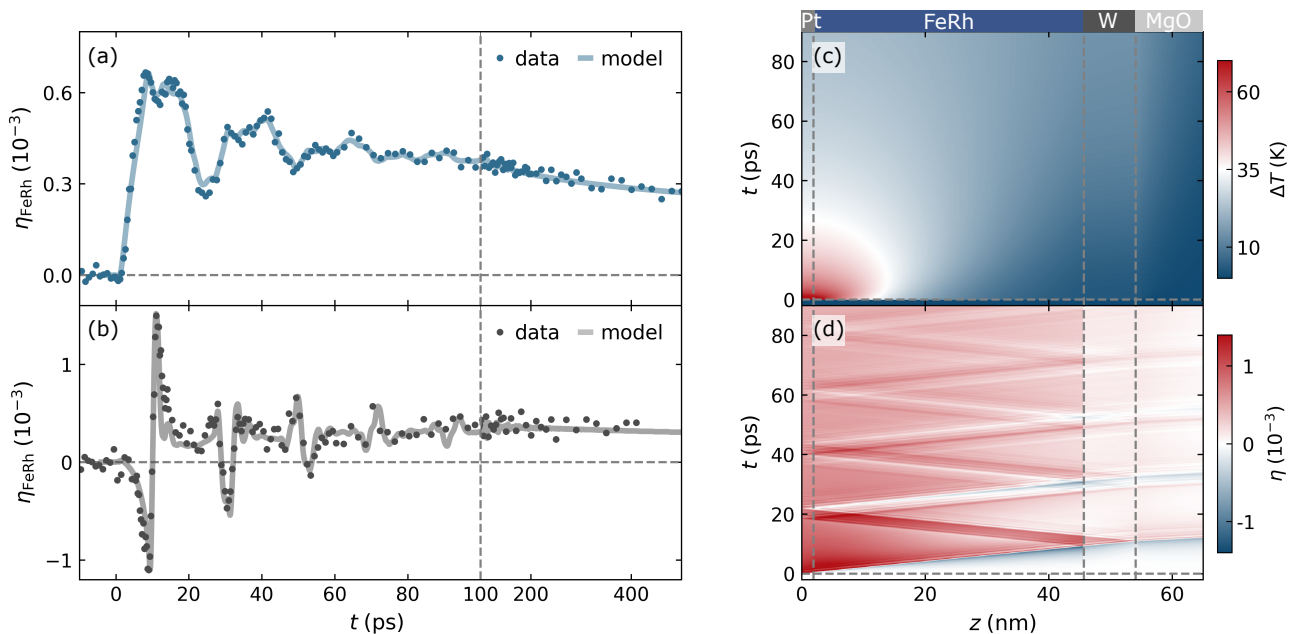


FIG. S1. **Results of modeling the strain response of FeRh and W utilizing the udkm1Dsim library:** Transient strain response of the FeRh layer (a) to an excitation of 1.6 mJ/cm^2 and of the W buffer layer (b) for a fluence of 6.3 mJ/cm^2 . The solid lines denote the modeled transient strain response for the respective fluences. The good agreement verifies the spatio-temporal temperature increase (c) and out-of-plane strain (d) for a fluence of 1.6 mJ/cm^2 determined by the heat diffusion equation within a 1TM and the one-dimensional elastic wave equation using the thermo-elastic parameters in Tab. S1.

S3. TEMPERATURE-DEPENDENT LASER-INDUCED AFM-FM PHASE TRANSITION

In this section, we present the dependence of the laser-induced FM volume fraction on the initial sample temperature of the 44 nm-thick FeRh film that complements the fluence-dependent study in the main text.

This experiment was performed at the KMC-3 XPP endstation of BESSY II in the low-alpha operation mode [23]. Its parallel and monochromatic x-ray beam in contrast to the convergent beam at the plasma x-ray source [24, 25] enables the separation of the FM and AFM Bragg peaks in reciprocal space. The FM and AFM Bragg peaks represent the increase of the lattice constant across the metamagnetic phase transition. Their integrated intensities serve as a quantitative measure of the respective volume fraction of both phases co-existing during the laser-driven phase transition. The clear separation of the peaks in the synchrotron experiment enables a parameter-free determination of the transient FM volume fraction, and hence a measure of the phase transition kinetics without parametrizing the temperature-dependent thermal expansion.

Figure S2(a) and (b) display the transient intensity distribution along the reciprocal q_z coordinate (symbols) encoding the out-of-plane lattice constant d via $q_z = 4\pi/d$ at 23 ps and 118 ps after excitation with a 600 fs laser pulse with a central wavelength of 1028 nm. The modeled intensity distribution (solid grey line) is the superposition of the AFM Bragg peak (blue) and the FM Bragg peak (green) at a larger lattice constant that emerges upon laser-excitation. Finally, the intensity distribution at each pump-probe delay yields V_{FM} by the integrated intensity of the FM Bragg peak with respect to the total diffracted intensity [26]. Figure S2(c) displays the transient V_{FM} at different initial sample temperatures ranging from 210 K to 330 K close to the transition temperature with a time-resolution of ≈ 15 ps given by the full-width half maximum of the x-ray pulse. We observe a similar behavior with increasing temperature as for increasing fluence in the main text. While the excitation well below the transition temperature only induces nucleation of FM domains on an 8 ps timescale, increasing the initial sample temperature enables the energy redistribution via heat transport to heat above the transition temperature which causes a growth of the nucleated FM domains into the depth of the film. As for high fluences, this results in a two-step rise of V_{FM} that becomes more dominant when approaching the transition temperature. These findings of a parameter free-extraction of V_{FM} support the interpretation in the main text.

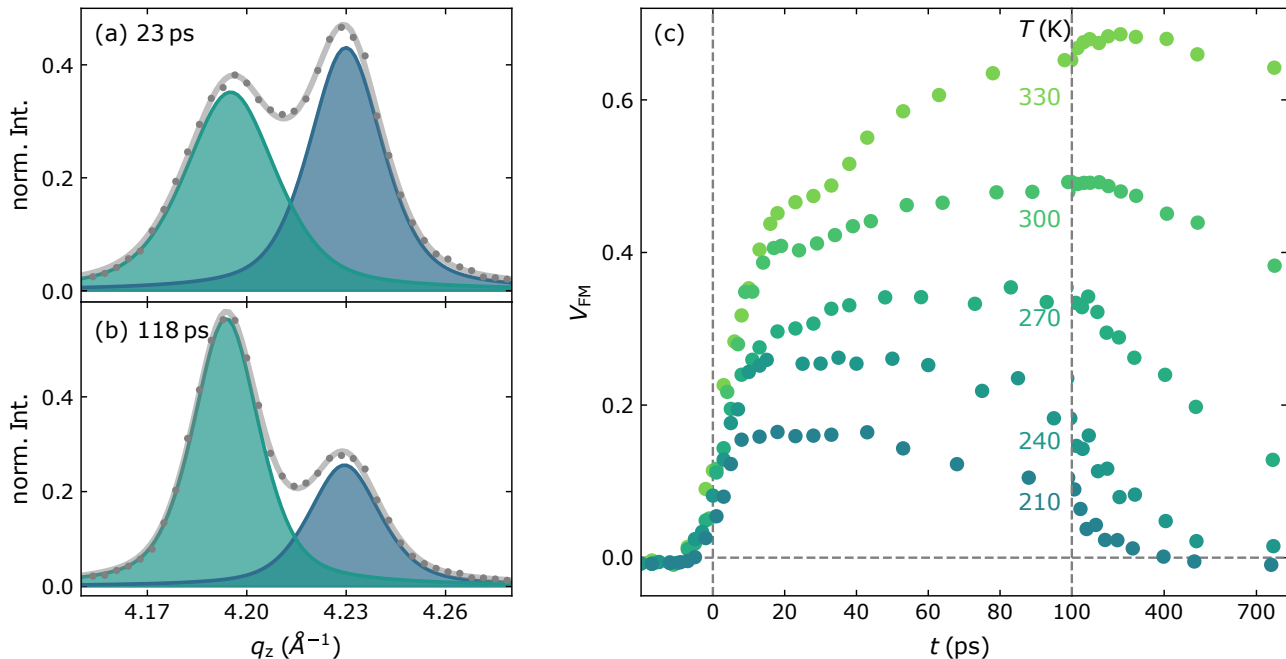


FIG. S2. **Two-step rise of FM volume fraction for excitation slightly below the transition temperature:** Transient rocking curve (grey) at 23 ps (a) and 118 ps (b) for an excitation of 6.5 mJ/cm^2 at 330 K separated into the Bragg peaks of the FM (green) and AFM phase (blue). In general, the integral of the Bragg peak is proportional to the fraction of the probed volume exhibiting the respective lattice structure. Therefore, the ratio of the integrated FM and AFM Bragg peak determines the transient FM volume fraction V_{FM} displayed for different initial sample temperatures in panel (c).

S4. FLUENCE-DEPENDENT MAGNETIZATION RISE FOR FRONT- AND BACKSIDE EXCITATION

Figure S3 presents the transient magnetization of the thick FeRh film from Fig. 3 in the main text normalized to its maximum. This representation for front- (a) and backside (b) excitation highlights the fluence dependence of the rise of the magnetization indicating the underlying kinetics of the AFM-FM phase transition. As a reference we additionally include the rise of the magnetization of the thin film as solid grey line. In frontside excitation geometry, the rise of the magnetization is independent from the fluence and in quantitative agreement with the behaviour of the thin film indicating optically induced nucleation in the near surface region of the thick FeRh film. In contrast, the rise of the magnetization at the sample surface after backside excitation becomes strongly fluence dependent and slows down with decreasing fluence. In addition, the magnetization rise is considerably slower than in the thin film and slightly delayed even for the highest fluence indicating the intrinsic kinetics of the domain growth driven by near-equilibrium heat transport. With increasing fluence less redistribution of the optically deposited energy density is required to heat the near-surface region above the transition temperature which speeds up the occurrence of the FM phase.

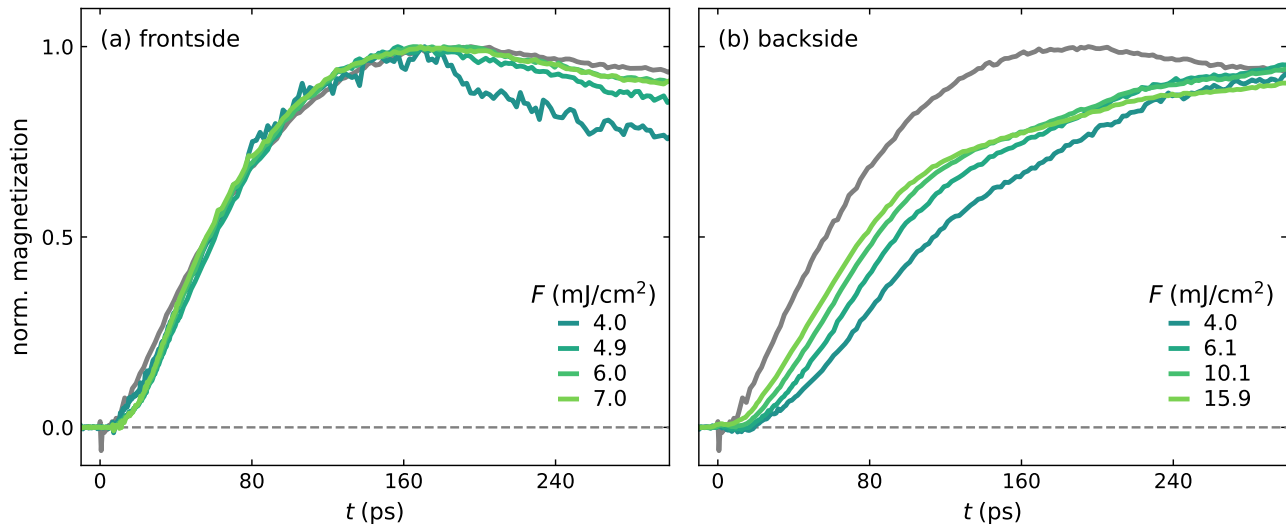


FIG. S3. **Fluence-dependent magnetization rise for front- and backside excitation:** Transient magnetization of the thick FeRh film from the main text normalized to the maximum in front- (a) and backside (b) excitation geometry for various fluences. The grey solid line denotes the rise of the normalized magnetization in the thin FeRh film. This representation highlights the fluence-independent rise for frontside excitation in quantitative agreement with the thin film and the decreasing speed of magnetization rise with decreasing fluence for backside excitation that is delayed in respect to the thin film dynamics originating from optically induced nucleation.

-
- [1] D. Schick, udkm1dsim—a python toolbox for simulating 1d ultrafast dynamics in condensed matter, *Computer Physics Communications* **266**, 108031 (2021).
 - [2] R. MacFarlane, J. Rayne, and C. Jones, Temperature dependence of elastic moduli of iridium, *Physics Letters* **20**, 234 (1966).
 - [3] S. Palmer, P. Dentschuk, and D. Melville, Elastic properties of an iron-rhodium alloy, *physica status solidi (a)* **32**, 503 (1975).
 - [4] F. H. Featherston and J. Neighbours, Elastic constants of tantalum, tungsten, and molybdenum, *Physical Review* **130**, 1324 (1963).
 - [5] M. A. Durand, The temperature variation of the elastic moduli of nacl, kcl and mgo, *Physical Review* **50**, 449 (1936).
 - [6] F. Nix and D. MacNair, The thermal expansion of pure metals. ii: molybdenum, palladium, silver, tantalum, tungsten, platinum, and lead, *Physical Review* **61**, 74 (1942).
 - [7] M. Ibarra and P. Algarabel, Giant volume magnetostriction in the ferh alloy, *Physical Review B* **50**, 4196 (1994).
 - [8] G. White and O. Anderson, Grüneisen parameter of magnesium oxide, *Journal of Applied Physics* **37**, 430 (1966).
 - [9] R. S. Krishnan, R. Srinivasan, and S. Devanarayanan, *Thermal expansion of crystals: international series in the science of the solid state* (Elsevier, 2013).

- [10] D. Zahn, H. Seiler, Y. W. Windsor, and R. Ernstorfer, Ultrafast lattice dynamics and electron–phonon coupling in platinum extracted with a global fitting approach for time-resolved polycrystalline diffraction data, *Structural Dynamics* **8**, 064301 (2021).
- [11] Z. Lin, L. V. Zhigilei, and V. Celli, Electron-phonon coupling and electron heat capacity of metals under conditions of strong electron-phonon nonequilibrium, *Physical Review B* **77**, 075133 (2008).
- [12] R. Shayduk, V. Vonk, B. Arndt, D. Franz, J. Stempffer, S. Francoual, T. F. Keller, T. Spitzbart, and A. Stierle, Nanosecond laser pulse heating of a platinum surface studied by pump-probe x-ray diffraction, *Applied Physics Letters* **109**, 043107 (2016).
- [13] M. Richardson, D. Melville, and J. Ricodeau, Specific heat measurements on an fe rh alloy, *Physics Letters A* **46**, 153 (1973).
- [14] G. K. White and S. Collocott, Heat capacity of reference materials: Cu and w, *Journal of physical and chemical reference data* **13**, 1251 (1984).
- [15] T. Barron, W. Berg, and J. Morrison, On the heat capacity of crystalline magnesium oxide, *Proceedings of the Royal Society of London. Series A. Mathematical and Physical Sciences* **250**, 70 (1959).
- [16] B. Bergman, G. Ju, J. Hohlfeld, R. J. van de Veerdonk, J.-Y. Kim, X. Wu, D. Weller, and B. Koopmans, Identifying growth mechanisms for laser-induced magnetization in ferh, *Physical Review B* **73**, 060407 (2006).
- [17] A. J. Slifka, B. J. Filla, and J. Phelps, Thermal conductivity of magnesium oxide from absolute, steady-state measurements, *Journal of research of the National Institute of Standards and Technology* **103**, 357 (1998).
- [18] M. Duggin, The thermal conductivities of aluminium and platinum, *Journal of Physics D: Applied Physics* **3**, L21 (1970).
- [19] Y. Chen, J. Ma, and W. Li, Understanding the thermal conductivity and lorenz number in tungsten from first principles, *Physical Review B* **99**, 020305 (2019).
- [20] L.-Y. Chen and D. W. Lynch, Ellipsometric studies of magnetic phase transitions of fe-rh alloys, *Physical Review B* **37**, 10503 (1988).
- [21] M. Mattern, A. von Reppert, S. P. Zeuschner, J.-E. Pudell, M. Herzog, and M. Bargheer, Concepts and use cases for picosecond ultrasonics with x-rays, arXiv preprint arXiv:2302.14116 [10.48550/ARXIV.2302.14116](https://arxiv.org/abs/2302.14116) (2023).
- [22] P. Algarabel, M. Ibarra, C. Marquina, A. Del Moral, J. Galibert, M. Iqbal, and S. Askenazy, Giant room-temperature magnetoresistance in the ferh alloy, *Applied physics letters* **66**, 3061 (1995).
- [23] M. Rössle, W. Leitenberger, M. Reinhardt, A. Koç, J. Pudell, C. Kwamen, and M. Bargheer, The time-resolved hard x-ray diffraction endstation kmc-3 xpp at bessy ii, *Journal of Synchrotron Radiation* **28**, 948 (2021).
- [24] D. Schick, A. Bojahr, M. Herzog, C. v. K. Schmising, R. Shayduk, W. Leitenberger, P. Gaal, and M. Bargheer, Normalization schemes for ultrafast x-ray diffraction using a table-top laser-driven plasma source, *Review of Scientific Instruments* **83**, 025104 (2012).
- [25] D. Schick, R. Shayduk, A. Bojahr, M. Herzog, C. v. Korff Schmising, P. Gaal, and M. Bargheer, Ultrafast reciprocal-space mapping with a convergent beam, *Journal of Applied Crystallography* **46**, 1372 (2013).
- [26] S. O. Mariager, F. Pressacco, G. Ingold, A. Caviezel, E. Möhr-Vorobeva, P. Beaud, S. Johnson, C. Milne, E. Mancini, S. Moyerman, *et al.*, Structural and magnetic dynamics of a laser induced phase transition in ferh, *Physical Review Letters* **108**, 087201 (2012).